Optics EXPRESS

Multi-mode plasmonic resonance broadband LWIR metamaterial absorber based on lossy metal ring

ZHENG QIN,[1,2,3] XIAOYAN SHI,[2,3] FUMING YANG,[2,3] ENZHU HOU,[1] DEJIA MENG,[2,4] CHUNFANG SUN,[1] RUI DAI,[1] SHOUTAO ZHANG,[1] HUA LIU,[1] HAIYANG XU,[1] AND ZHONGZHU LIANG[1,2,3,5]

[1] *Center for Advanced Optoelectronic Functional Materials Research and Key Laboratory of UV Light-Emitting Materials and Technology of Ministry of Education, College of Physics, Northeast Normal University, Changchun 130024, China*
[2] *State Key Laboratory of Applied Optics, Changchun Institute of Optics, Fine Mechanics and Physics, Chinese Academy of Sciences, Changchun, Jilin 130033, China*
[3] *University of the Chinese Academy of Sciences, China*
[4] *djmeng@sklao.ac.cn*
[5] *liangzz@nenu.edu.cn*

Abstract: Broadband perfect infrared wave absorption of unpolarized light over a wide range of angles in an ultrathin film is critical for applications such as thermal emitters and imaging. Although many efforts have been made in infrared broadband absorption, it is still challenging to cover the perfect absorption of broadband in the long-wave infrared band. We propose a long-wave infrared broadband, polarization, and incident angle insensitivity metamaterial absorber based on the supercell with four rings of two sizes. Broadband absorption covering the long-wave infrared band is realized by combining four PSPRs and LSPRs absorption peaks excited by the supercell structure. The absorptivity of our absorber exceeds 90% in the wavelength range of 7.76~14μm, and the average absorptivity reaches 93.8%. The absorber maintains more than 80% absorptivity as the incident angle of unpolarized light reaches 60°, which may have promising applications for thermal emitters, infrared imaging, thermal detection.

1. Introduction

The periodic or quasi-periodic artificial two-dimensional structure composed of sub-wavelength nano-micron arrays provides a powerful and compact platform for light manipulation [1,2]. It can achieve novel functions that are not available in natural materials, such as near-field enhancement [3], perfect absorption [4], induced transparency [5], metalens [6], and optical stealth [7]. Among them, metamaterial absorbers (MA) based on a patterned metal-dielectric-metal sandwich structure have received extensive attention [4,8,9]. Light absorption is an important performance index of optical devices. The ability of natural materials to absorb incident light depends on their thickness, and their bandgap limits the response wavelength. In the infrared band, incident light is either strongly reflected (metal) or completely transmitted (dielectric), and materials with high absorption are scarce. The MA breaks through the limitations of natural materials and can achieve perfect absorption of any target wavelength through properly designing its geometric parameters [9–11]. Its sub-wavelength-scale light field confinement capability and a thickness much smaller than the wavelength make it an ideal choice for solar energy harvesting [12], thermal emitters [13], photodetectors [14,15], photothermal switches [16], gas detection [17,18], and thermal imaging [19,20]. However, the resonant nature of plasmon excitation limits the absorption bandwidth. Since general MAs can only achieve perfect absorption in a narrow wavelength range, it is still

#446655 https://doi.org/10.1364/OE.446655
Journal © 2022 Received 26 Oct 2021; revised 28 Nov 2021; accepted 5 Dec 2021; published 21 Dec 2021

challenging to meet the requirements of broadband response in practical applications, especially in the long-wave infrared band.

The general method to obtain broadband absorption is to use a grating or three-dimensional pyramid structure with multi-metal-dielectric layers [21–25]. For example, Zhou et al. demonstrated an Au-Ge multilayer structure that achieves broadband absorption in mid-wave infrared [22]; Zhang et al. showed a VO_2-Ge multilayer structure that achieves broadband absorption in the visible-near infrared and long-wave infrared bands [26]. However, this solution inevitably increases the total thickness and the difficulty of fabrication and limits the integration of the MA on the existing nanophotonic devices. Coplanar resonator design is another solution to achieve broadband absorption [27]. Using cross-shaped or circular resonators of multiple sizes can excite multiple localization plasmon resonances (LSPRs) with similar wavelengths. Resonator and absorption peaks correspond one by one, and several absorption peaks combine to broadband absorption. However, the absorption cross-section of each resonator is limited, and the combination of multiple resonators increases the effective period of each resonator, resulting in a decrease in the overall absorption performance. Our previous work proposed a hybrid dielectric layer scheme using lossy dielectric such as silicon nitride and silicon dioxide successfully achieved broadband absorption covering long-wave infrared and very long-wave infrared [28,29]. The disadvantage of this scheme is that the working band depends on the intrinsic absorption of the lossy dielectric. It is necessary to add a lossless dielectric between the resonator and the lossy dielectric layer to overcome the performance degradation at the wavelength where Im(ε) of the lossy dielectric is too high [30]. The lossy dielectric layer absorbs considerable part energy of the incident light also limits the application of this scheme to a certain extent. Overall, this scheme makes the design of MA be challenging and limits the selection of the dielectric layer.

Here we propose a multi-mode plasmonic resonance broadband LWIR metamaterial absorber. Firstly, we propose a metal-dielectric-metal sandwich named composite structure that equips with an array with alternating two-size lossy metal rings. The composite structure absorber exhibits a triple-peak broadband absorption of long-wave infrared due to exciting propagating surface plasmon resonance (PSPR) and two LSPRs. Next, we analyzed the influence of the absorber's geometric parameters on its performance. Subsequently, we improved the composite structure and obtained the supercell structure by reducing the distance between four adjacent rings. This supercell structure has one more absorption peak caused by PSPR than the composite structure, which achieves broadband absorption covering the long-wave infrared band and exhibits polarization insensitivity and incident angle insensitivity. The energy of the incident light is absorbed by the metal so that the dielectric layer can be flexibly selected. Our MA can be used in radiation cooling, thermal imaging, and other fields.

2. Result and discussion

Figure 1(a) shows the schematic diagram of our proposed MA. The MA comprises a metal plane bottom and ring array, and a dielectric layer fills in the space. The metal ring array is composed of two different sizes arranged alternately. The following geometric parameters characterize the structure of the MA: The thickness of the resonator, dielectric layer, the bottom layer is denoted by h, d, t respectively, the outer and inner radius of the ring is denoted by R and r, and period is p. The dielectric layer used here is amorphous silicon, and the metal is the lossy metal titanium. Titanium and silicon can be prepared by magnetron sputtering or electron beam evaporation. The upper array can be prepared by existing nano-processing methods such as electron beam lithography (EBL) and nanoimprinting. We performed a simulation using the Finite Difference Time Domain (FDTD) method to verify the absorber performance. The optical parameters of silicon and titanium come from Palik [31] and Rakić [32]. The light is incident perpendicularly along the negative direction of the z-axis, and the polarization direction is along the x-axis.

Optics EXPRESS

Periodic boundary conditions are used in x and y directions, and PML boundary is used in z-direction. We set geometric parameters of the absorber as h=100nm, d=620nm, t=200nm, p=2.4μm, R_1=500nm, R_2=700nm, r_1=300nm, r_2=400nm. The total thickness of our absorber is 920nm, less than one-tenth of the central working wavelength. We believe that the results from the simulation of the periodic boundary conditions here can represent the performance of the finite array sizes in practical applications because previous work proves that the performance of as few as 4*4 arrays is similar to the infinite arrays [33].

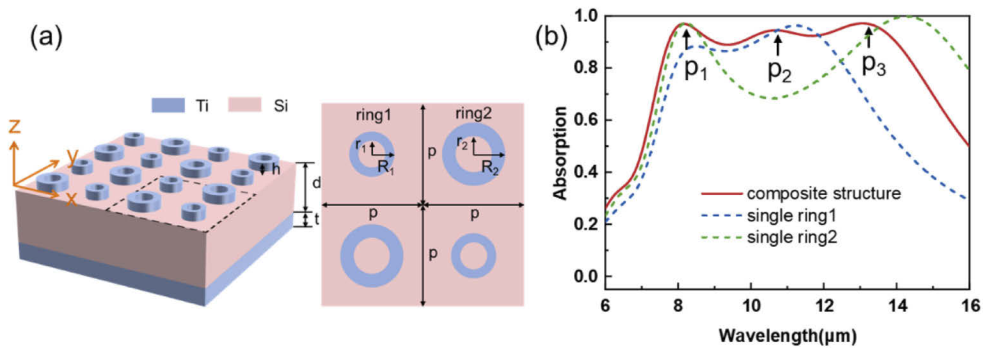

Fig. 1. (a) Schematic diagram of the structure of the metamaterial absorber, which consists of a titanium bottom and titanium resonator array separated by a dielectric layer. Its geometric parameters are: h=100 nm, d=620 nm, t=200 nm, p=2.4μm, R_1=500 nm, R_2=700 nm, r_1=300 nm, r_2=400 nm. (b) The absorption spectrum of the absorber.

The absorption spectrum of the absorber is calculated from the reflectance and transmittance obtained by simulation, A=1-R-T. The solid red line in Fig. 1(b) shows that the absorber has three absorption peaks in the simulated waveband, located at 8.16μm, 10.6μm, and 13.1μm, marked as p_1, p_2, and p_3, and the absorptivity reached 96.5%, 94%, and 97.1% respectively. We also calculated the absorption spectra of the two sizes of resonators when they exist alone, represented by blue and green dashed lines. Figure 1(b) shows two absorption peaks in the blue (green) dotted line. The absorption peak on the left coincides with p_1 of the composite structure, and the absorption peak on the right is red-shifted relative to the p_2 (p_3) of the composite structure.

To explain the physical mechanism that causes perfect absorption, we calculated the distribution of the magnetic field at the wavelengths of the three absorption peaks. As shown in Fig. 2(a), the magnetic field at p_1 is concentrated in the dielectric layer below the two sides of the adjacent resonators, indicating that PSPR is excited [34]. As shown in Fig. 2(b), the magnetic field at p_2 is concentrated under the ring_1 resonator on the left, indicating that ring_1 excites the LSPR [35]. The magnetic field at p_3 is concentrated under the ring_2 resonator on the right, indicating that ring_2 excites PSPR. Therefore, the broadband absorption of our proposed composite resonator structure absorber is caused by the hybrid mode of PSPR and LSPR.

To analyze the influence of the geometric parameters of the absorber on its performance, we used a single-size ring structure for simulation calculations. As shown in Fig. 3(a), the inner radius and outer radius of the single-size ring are 400nm and 600nm, respectively, and other parameters remain the same with the composite structure. We can see that the single-size structure has two absorption peaks, located at the wavelengths of 8.6 μm and 12.8 μm, which are marked as m_1 and m_2 in Fig. 3(a), and the absorptivity are 97.9% and 99.3%, respectively. The magnetic field distributions at the two absorption peaks are shown in the left part of Fig. 3(c) and Fig. 3(f). It can be seen that m_1 is the PSPR mode, and m_2 is the LSPR mode. Figure 3(d) and (e) show the electric field distribution on the xoz plane and xoy plane at m_1, respectively. Figure 3(g) and (h) show the electric field distribution on the xoz plane and xoy plane at m_2,

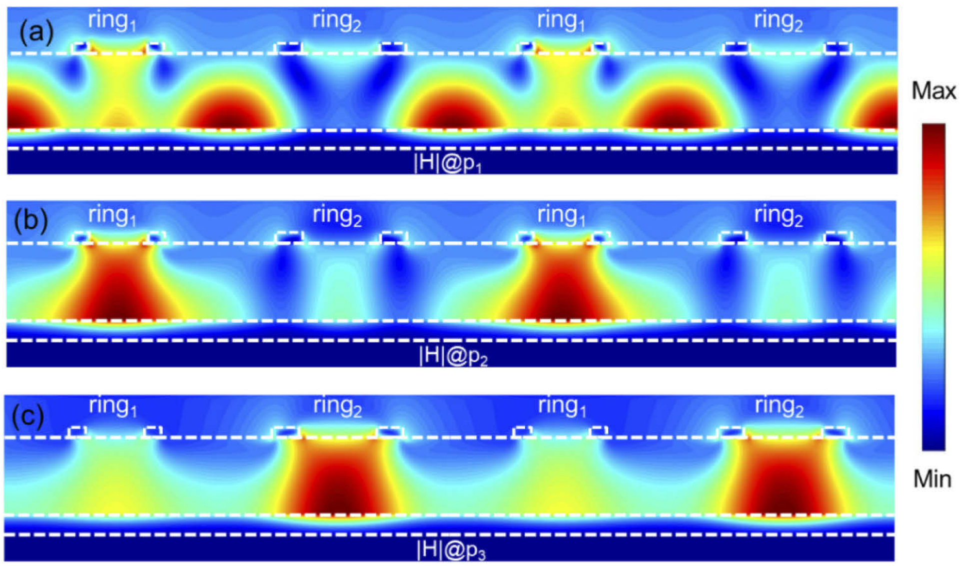

Fig. 2. The magnetic field distribution at the absorption peak, (a) field distribution at p_1, (b) field distribution at p_2, (c) field distribution at p_3.

respectively. Although the electric field is concentrated at the edge of the ring resonator at the two absorption peaks, the intensity of the electric field at m_2 is much stronger than that at m_1, indicating that the two modes have different confinement capabilities to the electric field. At the same time, we also show the current distributions at the two absorption peaks in Fig. 3(d) and Fig. 3(g). a positive electrode and a negative electrode are formed at the two ends of the ring resonator, and the lower dielectric-bottom metal interface included continuous current illustrates the transmission of electrons at the interface. At m_1, the current is unidirectionally transmitted at the lower dielectric-metal interface, and positive and negative electrodes are formed at both ends of the resonator(no obvious orientation on the xoz plane). At m_2, the anti-parallel current between the upper ring resonator and the bottom metal formed a loop, which causes the magnetic field to be concentrated between the two layers of metal, so the first-order LSPR is also called magnetic polariton resonance (MPR) mode [36].

The influence of the geometric parameters of the absorber on its PSPR can be expressed as [37]:

$$\lambda_{PSP} = \frac{P}{\sqrt{i^2 + j^2}} \sqrt{\frac{\varepsilon_m \varepsilon_d}{\varepsilon_m + \varepsilon_d}} \tag{1}$$

where P is the period of the absorber, ε_m and ε_d represent the permittivity of metal and dielectric. As is shown in Fig. 3(b), the LSPR mode can be explained by the equivalent circuit theory [36]:

$$\lambda_{LSP} = 2\pi c\sqrt{LC/2} \tag{2}$$

where L is the equivalent inductance of the absorber, which compose two parts:

$$L = L_m + L_e \tag{3}$$

Here $L_m = \frac{\beta_1 \mu_0 d}{2}$ represents the inductance between the resonator and the metal bottom, and β_1 is the effective coefficient. $L_e = \frac{1}{\delta\omega^2\varepsilon_0}\left(\frac{\varepsilon_m'^{\,2}}{\varepsilon_m'} + \varepsilon_m''^{2}\right)$ represents the contribution of drifting electrons to inductance. μ_0 is vacuum permeability and ε_0 vacuum permittivity and δ represent

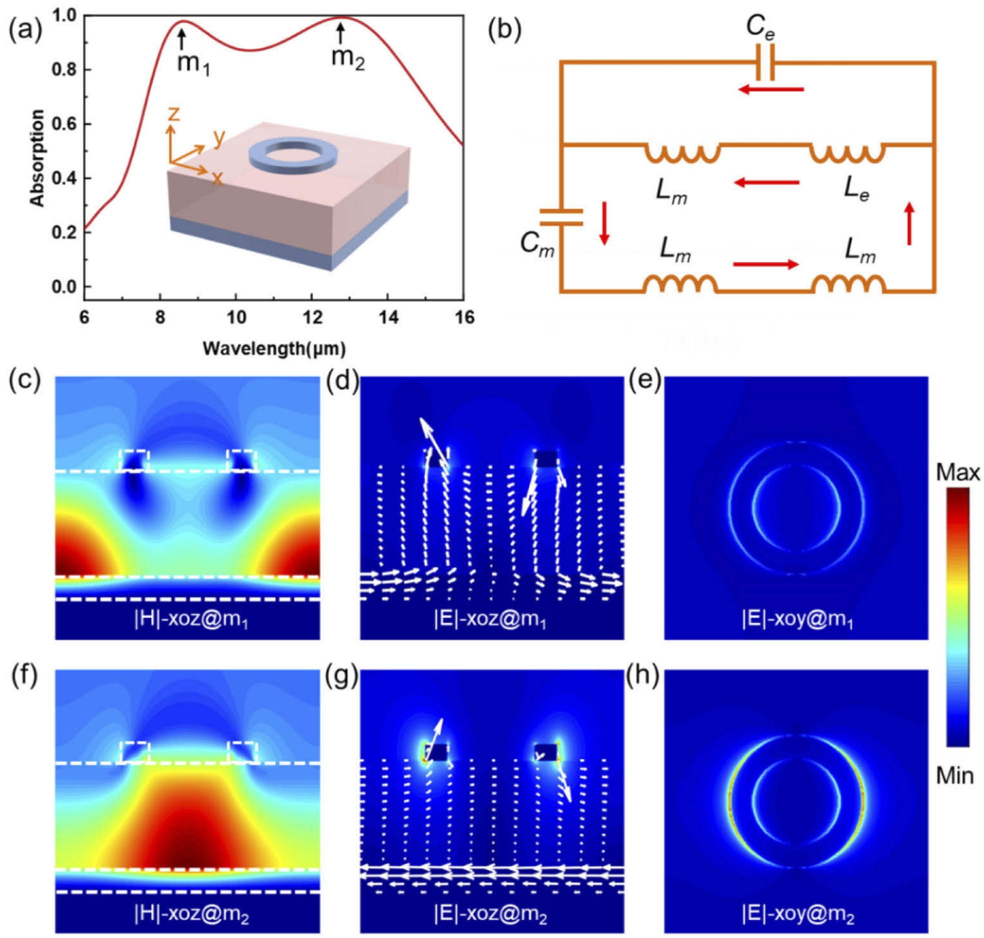

Fig. 3. (a) The absorption spectrum of the single-size ring structure (inset is a schematic diagram of the single-size ring structure). (b) Schematic of the equivalent LC circuit for LSPR mode. (c) The magnetic field distribution in xoz plane at mode$_1$. (d) The electronic field distribution and current distribution in xoz plane at mode$_1$. (e) The electronic field distribution in xoy plane at mode$_1$. (f) The magnetic field distribution in xoz plane at mode$_2$. (g) The electronic field distribution and current distribution in xoz plane at mode$_2$. (h)The electronic field distribution in xoy plane (right) at mode$_2$.

the penetration depth of the metal. C is the equivalent capacitance of the absorber, which compose two parts:

$$C = C_e + C_m \tag{4}$$

Here $C_m = \frac{c_1 \varepsilon_0 \varepsilon_d A}{dn}$ represents the capacitance between the resonator and the bottom, $A = \pi(R^2 - r^2)$ is the area of the resonator, and c_1 is effective coefficient represents the effective area of the resonator corresponding to the metal bottom. $C_e = \frac{c_2 \varepsilon_0 t_m 2R}{P - 2R'}$ represents the capacitance between the adjacent resonators, c_2 is effective coefficient represents the effective area between adjacent resonators, $2R' \propto R - r$ represents the effective width of the ring resonator.

Next, we calculated the dependence of the absorber's performance on its geometric parameters. As shown in Fig. 4, the blue (red) line shows the dependence of m_1 (m_2) on the period, the inner radius, and the outer radius of the ring resonator. In addition to changes in parameters shown in the figure, the remaining parameters are the same as those in Fig. 3(a). Figure 4(a) shows that

Optics EXPRESS

m_1 redshifts as the period become larger, which is in line with the prediction of formula (1). Figure 4(b) and (c) respectively show that m_1 redshifts as the inner radius increases, and blue shifts as the outer radius increases. This is because the equivalent period of the exciting PSPR is $p_{eff} = p - k_1 R + k_2 r$, where k_1 and k_1 are the effective coefficients, the change in the resonator's inner radius and outer radius affects the equivalent period and then causes the position shift of m_1. The red line in Fig. 4(a) shows that m_2 blue shifts as the period increases. This is because the increase in period reduces the capacitance between adjacent resonators, causing the blue shift of the absorption peak. Figure 4(b) shows that as the inner radius of the resonator increases, m_2 has a weak redshift. This is because the increase in the inner radius reduces C_m while increasing C_e, the total capacitance increases slightly. Figure 4(c) shows a significant red shift of m_2 as the outer radius of the resonator increases due to the capacitance between the adjacent resonators increasing as the outer radius increases. Therefore, we can manipulate the two absorption peaks relatively independently. For example, we can simultaneously increase the outer and inner radius to redshift m_2 while keeping m_1 unchanged. This manipulation is difficult to achieve on circular and square resonators.

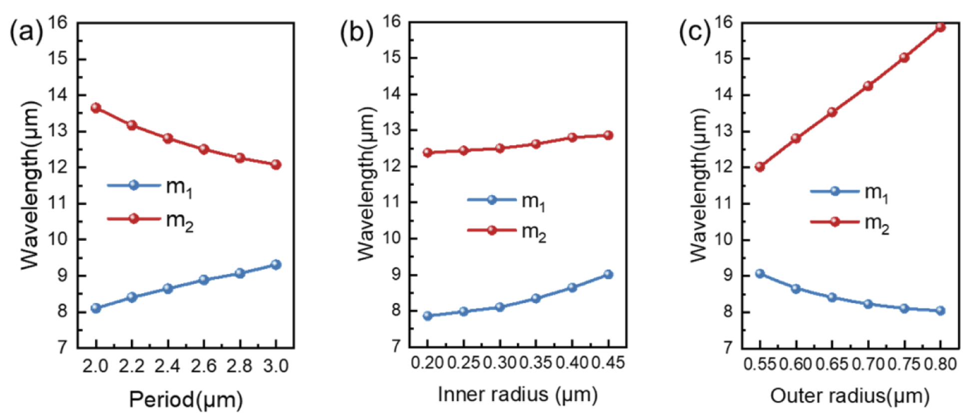

Fig. 4. the dependence of the absorber's performance on its geometric parameters: (a) period, (b) inner radius, (c)outer radius.

Based on the above analysis, we can explain the displacement of the absorption peak corresponding to the composite structure and the single-size structure in Fig. 1(b). First, the p_1 of the composite structure and the left absorption peak of the single-size ring structure almost overlap. This is because the positions of the left absorption peaks of the two single-size ring structures are similar, and the composite structure maintains symmetry. For the PSPR mode, the period hardly changes. Compared with the two single-size ring structures represented by the yellow and green dashed lines in Fig. 1(b), the absorption peaks of the composite structure p_2 and p_3 have different degrees of blue shift. It shows that the result of the interphase arrangement has a significant effect on the LSPR. Due to the composite structure making the distance between adjacent same-size resonators larger, for the LSPR mode, it is equivalent to a larger period. This is also the limitation of using multi-size resonators to excite LSPRs to achieve broadband absorption.

The composite structure in Fig. 1(a) achieves a broadband absorption with three absorption peaks for long-wave infrared. Despite this, there is still a weak dip between the two absorption peaks of p_1 and p_2, making the absorptivity less than 90%. In the previous analysis, we find that the absorption peak caused by PSPR mode is less affected by the ring size change, so we consider changing the distance between four adjacent resonators to form a supercell structure with four resonators to generate a new absorption peak. As shown in Fig. 5(a), the period of the supercell

Optics EXPRESS

structure is 2p=4.8μm, which is consistent with the period of the composite structure, and the distance between adjacent resonators in the supercell is g=2.2μm, which is slightly smaller than p. Other parameters keep consistent with the composite structure. Figure 5(b) shows the absorption spectrum (solid red line) of the supercell structure. It can be seen that the absorption spectrum entirely coincides with the composite structure (solid grey line) except for a new absorption peak p_4 at the wavelength of 9.3μm, indicating that the slight damage to the symmetry of the resonator arrangement does not affect the original resonance mode. Here the absorptivity of p_4 has increased from 88% to 94.1%. The absorptivity of the supercell structure in the wavelength range of 7.76 to 14 μm exceeds 90%, and the average absorptivity in this wavelength range reaches 93.8%.

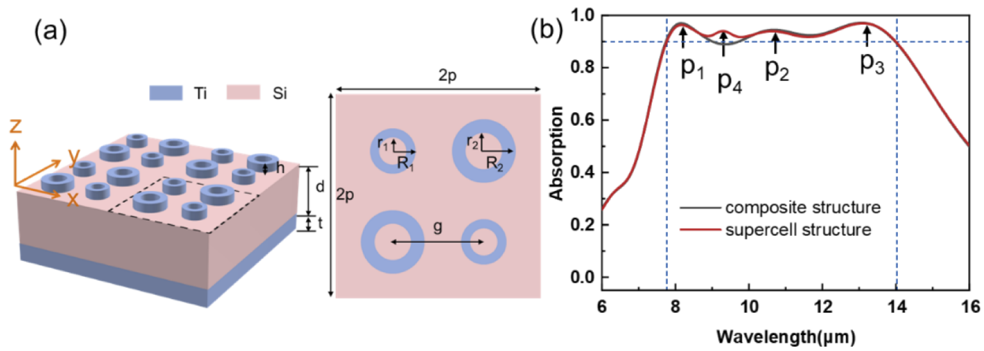

Fig. 5. (a) A schematic diagram of the supercell structure consists of a titanium bottom and titanium resonator array separated by a dielectric layer. Its geometric parameters are: h=100 nm, d=620 nm, t=200 nm, p=2.4μm, g=2.2μm, R_1=500 nm, R_2=700 nm, r_1=300 nm, r_2=400 nm. (b) The absorption spectrum of the supercell structure absorber.

Figure 6(a) shows the magnetic field distribution at the absorption peak p_4. It can be seen that the magnetic field is mainly distributed in the dielectric layers outside of the two resonators. At the same time, there is also apparent distribution under $ring_1$, indicating the absorption peak p_4 is caused by the hybrid mode of PSPR and LSPR. It should be noted that, unlike the situation at p_1, the PSPR here is excited by the supercell. Figure 6(b) shows the magnetic field distribution at the aforementioned composite structure's corresponding wavelength(9.3μm). It can be seen that the magnetic field is mainly distributed under $ring_1$, and the intensity is less than p_3, indicating that LSPR is excited at this condition. Comparing Fig. 6(a) and (b), we know that our supercell structure breaks the symmetry of the adjacent resonator, which makes the ring array one more period, excites a new PSPR. The effective period here is less than 4.8μm, and the hybridization with the LSPR makes the wavelength of the absorption peak quite different from the formula calculation.

For long-wave infrared absorbers, the energy from the incident light is eventually converted into heat and dissipated inside the absorber. The form and distribution of heat dissipation are different for different absorber structures. For example, the heat of the dielectric-metal multilayer structure is often concentrated in separate layers by wavelength. For MAs, it is usually a local hot spot [15]. Here we calculated the absorption distribution in the MA using:

$$\mathrm{Q}(\omega) = \frac{1}{2} \times \omega \times \varepsilon'' \times |E(\omega)|^2 \tag{5}$$

where ε'' is the imaginary part of permittivity, and $E(\omega)$ is the local electric field. Figure 7(a) shows the heat distribution at p_1. We can see that the heat is concentrated in the bottom on the outside and middle of two resonators, and ring1. We can see in Fig. 7(b) that heat distribution at

Optics EXPRESS

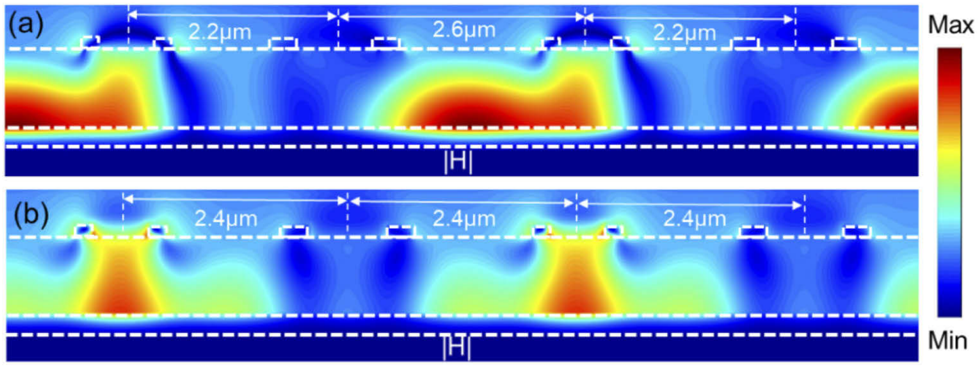

Fig. 6. (a)The magnetic field distribution at p_4(9.3μm) of the supercell structure, (b) The magnetic field distribution at 9.3μm of the composite structure.

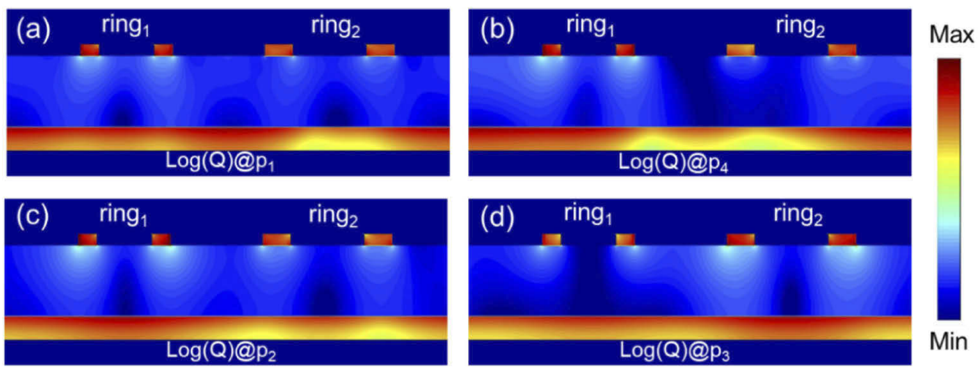

Fig. 7. The cross-view heat distribution of supercell absorber at (a) p_1, (b) p_2, (c) p_3, (d) p_4.

p_4 is concentrated in the bottom outside of the two rings and in $ring_1$. Heat distribution in $ring_1$ at p_4 is much stronger than p1, and there is almost no distribution on the bottom between the two rings. This is the result of coupling between the PSPR excited by the supercell structure and the LSPR excited by $ring_1$. Figure 7(c) and (d) show the heat distribution of the LSPR excited by the two resonators, respectively. Figure 7(c) shows that at p_2, heat is mainly distributed in $ring_1$ and the bottom below it. Figure 7(d) shows that at p_3, the energy is distributed primarily in $ring_2$ and the bottom below it. The metal layer absorbs the energy of the incident light at all four absorption peaks so that we can choose the dielectric layer flexibly.

Existing infrared devices often work under a larger incident angle, so the absorber is required to maintain high absorption for unpolarized light within a wild incident angle range. As shown in Fig. 8(a), when the polarization angle of the incident light gradually changes from 0° to 90°, there is almost no change in the absorption spectrum, showing polarization insensitivity, which benefits from the symmetry of our supercell structure. Figure 8(b) and (d) indicate that our absorber is insensitive to the incident angle. The TM wave and TE wave definitions are shown in the insets in Fig. 8(b) and (d). We can see in Fig. 8(b) that when the incident angle of the TM wave reaches 60°, the absorber still maintains more than 90% absorption. For TE waves, as Fig. 8(d) shows, when the incident angle reaches 60°, despite the depression, the average absorptivity of the absorber remains above 70%. For unpolarized light, the absorber maintains an average absorptivity exceeds 80% in the long-wave infrared when the incident angle reaches 60° (Fig. 8(c)), showing excellent angle insensitivity.

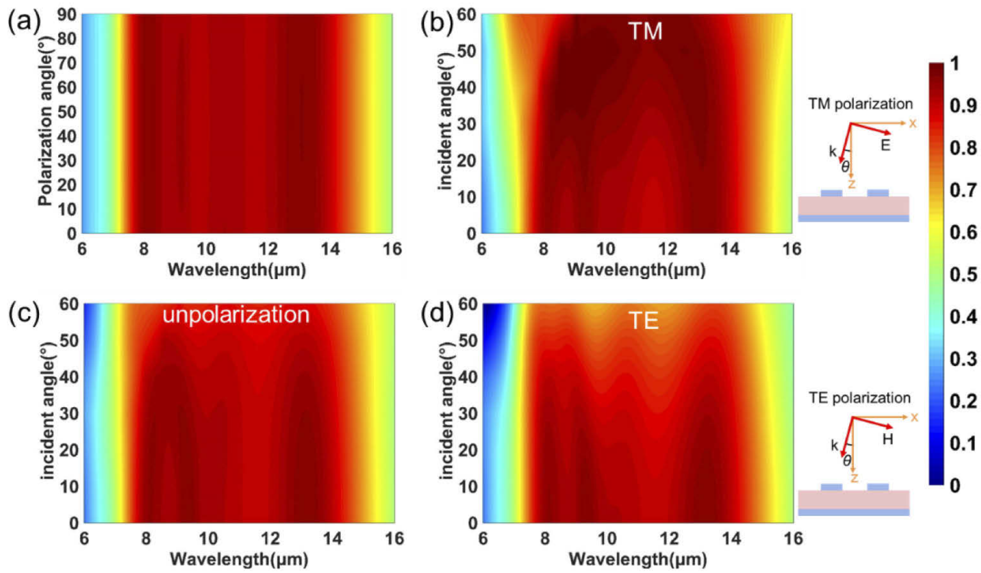

Fig. 8. The dependence of the absorber's performance on the (a) polarization angle, (b) TM wave incident angle, (c) unpolarized wave incident angle (d) TE wave incident angle.

3. Conclusion

In summary, we proposed a long-wave infrared broadband, polarization insensitivity, and incident angle insensitivity metamaterial absorber based on the supercell with four rings of two sizes. First, we proposed a metal-dielectric-metal three-layer absorber composed of an array of rings arranged alternately in two sizes. This composite structure achieves broadband absorption of three peaks in the long-wave infrared band. Field distribution analysis shows that the three absorption peaks caused by PSPR co-excited by two rings and two LSPRs, respectively excited by them. Then we analyzed the manipulation of the geometrical parameters of the absorber's performance. Then we proposed a supercell structure composed of four rings, which was obtained by reducing the distance between four adjacent rings in the composite structure. Compared with the composite structure, the supercell structure excites one more PSPR and has one more absorption peak. The absorptivity of the supercell structure exceeds 90% in the wavelength range of 7.76~14μm, and the average absorptivity reaches 93.8%. We analyzed the energy absorption distribution at the four peaks and found that it was mainly concentrated in the metal layer, indicating we can optionally select dielectric. The absorber we proposed also shows insensitivity to polarization and incident angle. When the unpolarized incident angle reaches 60°, the absorptivity is still more than 80%. The absorber we designed may have promising applications for infrared imaging, thermal detection, radiation cooling.

Funding. National Natural Science Foundation of China (61735018, 61805242); Jilin Scientific and Technological Development Program (20190103014JH); Excellent Member of Youth Innovation Promotion Association of the Chinese Academy of Sciences (2014193, Y201836); Leading Talents and Team Project of Scientific and Technological Innovation for Young and Middle-aged Groups in Jilin Province (20190101012JH).

Disclosures. The authors declare no conflicts of interest.

Data availability. Data underlying the results presented in this paper are not publicly available at this time but may be obtained from the authors upon reasonable request.

References

1. K. Dixon, A. O. Montazeri, M. Shayegannia, E. S. Barnard, S. Cabrini, N. Matsuura, H. Y. Holman, and N. P. Kherani, "Tunable rainbow light trapping in ultrathin resonator arrays," Light: Sci. Appl. **9**(1), 194 (2020).

2. Z. Xuan, J. Li, Q. Liu, F. Yi, S. Wang, and W. Lu, "Artificial Structural Colors and Applications," The Innovation **2**(1), 100081 (2021).
3. A. John-Herpin, D. Kavungal, L. von Mucke, and H. Altug, "Infrared Metasurface Augmented by Deep Learning for Monitoring Dynamics between All Major Classes of Biomolecules," Adv. Mater. **33**(14), 2006054 (2021).
4. P. Yu, L. V. Besteiro, Y. Huang, J. Wu, L. Fu, H. H. Tan, C. Jagadish, G. P. Wiederrecht, A. O. Govorov, and Z. Wang, "Broadband Metamaterial Absorbers," Adv. Opt. Mater. **7**(3), 1800995 (2019).
5. J. Gu, R. Singh, X. Liu, X. Zhang, Y. Ma, S. Zhang, S. A. Maier, Z. Tian, A. K. Azad, H. T. Chen, A. J. Taylor, J. Han, and W. Zhang, "Active control of electromagnetically induced transparency analogue in terahertz metamaterials," Nat. Commun. **3**(1), 1151 (2012).
6. S. Shrestha, A. C. Overvig, M. Lu, A. Stein, and N. Yu, "Broadband achromatic dielectric metalenses," Light: Sci. Appl. **7**(1), 85 (2018).
7. H. X. Xu, G. Hu, Y. Wang, C. Wang, M. Wang, S. Wang, Y. Huang, P. Genevet, W. Huang, and C. W. Qiu, "Polarization-insensitive 3D conformal-skin metasurface cloak," Light: Sci. Appl. **10**(1), 75 (2021).
8. C. M. Watts, X. Liu, and W. J. Padilla, "Metamaterial electromagnetic wave absorbers," Adv. Mater. **24**(23), OP98–OP120 (2012).
9. N. I. Landy, S. Sajuyigbe, J. J. Mock, D. R. Smith, and W. J. Padilla, "Perfect metamaterial absorber," Phys. Rev. Lett. **100**(20), 207402 (2008).
10. N. Liu, M. Mesch, T. Weiss, M. Hentschel, and H. Giessen, "Infrared perfect absorber and its application as plasmonic sensor," Nano Lett. **10**(7), 2342–2348 (2010).
11. L. Guo, X. Ma, Y. Zou, R. Zhang, J. Wang, and D. Zhang, "Wide-angle infrared metamaterial absorber with near-unity absorbance," Opt. Laser Technol. **98**, 247–251 (2018).
12. C. C. Chang, W. J. M. Kort-Kamp, J. Nogan, T. S. Luk, A. K. Azad, A. J. Taylor, D. A. R. Dalvit, M. Sykora, and H. T. Chen, "High-Temperature Refractory Metasurfaces for Solar Thermophotovoltaic Energy Harvesting," Nano Lett. **18**(12), 7665–7673 (2018).
13. N. Lee, T. Kim, J. S. Lim, I. Chang, and H. H. Cho, "Metamaterial-Selective Emitter for Maximizing Infrared Camouflage Performance with Energy Dissipation," ACS Appl. Mater. Interfaces **11**(23), 21250–21257 (2019).
14. H. Gao, Y. Liang, L. Yu, S. Chu, L. Cai, F. Wang, Q. Wang, and W. Peng, "Bifunctional plasmonic metamaterial absorber for narrowband sensing detection and broadband optical absorption," Opt. Laser Technol. **137**, 106807 (2021).
15. W. Li and J. Valentine, "Metamaterial perfect absorber based hot electron photodetection," Nano Lett. **14**(6), 3510–3514 (2014).
16. Z. Qian, S. Kang, V. Rajaram, C. Cassella, N. E. McGruer, and M. Rinaldi, "Zero-power infrared digitizers based on plasmonically enhanced micromechanical photoswitches," Nat. Nanotechnol. **12**(10), 969–973 (2017).
17. A. Lochbaum, A. Dorodnyy, U. Koch, S. M. Koepfli, S. Volk, Y. Fedoryshyn, V. Wood, and J. Leuthold, "Compact Mid-Infrared Gas Sensing Enabled by an All-Metamaterial Design," Nano Lett. **20**(6), 4169–4176 (2020).
18. X. Tan, H. Zhang, J. Li, H. Wan, Q. Guo, H. Zhu, H. Liu, and F. Yi, "Non-dispersive infrared multi-gas sensing via nanoantenna integrated narrowband detectors," Nat. Commun. **11**(1), 5245 (2020).
19. K. Fan, J. Y. Suen, X. Liu, and W. J. Padilla, "All-dielectric metasurface absorbers for uncooled terahertz imaging," Optica **4**(6), 601–604 (2017).
20. A. Tittl, A. K. Michel, M. Schaferling, X. Yin, B. Gholipour, L. Cui, M. Wuttig, T. Taubner, F. Neubrech, and H. Giessen, "A Switchable Mid-Infrared Plasmonic Perfect Absorber with Multispectral Thermal Imaging Capability," Adv. Mater. **27**(31), 4597–4603 (2015).
21. Y. Cui, K. H. Fung, J. Xu, H. Ma, Y. Jin, S. He, and N. X. Fang, "Ultrabroadband light absorption by a sawtooth anisotropic metamaterial slab," Nano Lett. **12**(3), 1443–1447 (2012).
22. J. Zhou, A. F. Kaplan, L. Chen, and L. J. Guo, "Experiment and Theory of the Broadband Absorption by a Tapered Hyperbolic Metamaterial Array," ACS Photonics **1**(7), 618–624 (2014).
23. N. T. Q. Hoa, P. H. Lam, P. D. Tung, T. S. Tuan, and H. Nguyen, "Numerical Study of a Wide-Angle and Polarization-Insensitive Ultrabroadband Metamaterial Absorber in Visible and Near-Infrared Region," IEEE Photonics J. **11**(1), 1–8 (2019).
24. Y.-L. Liao, Y. Zhao, S. Wu, and S. Feng, "Wide-angle broadband absorber based on uniform-sized hyperbolic metamaterial," Opt. Mater. Express **8**(9), 2484–2493 (2018).
25. Q. Liang, T. Wang, Z. Lu, Q. Sun, Y. Fu, and W. Yu, "Metamaterial-Based Two Dimensional Plasmonic Subwavelength Structures Offer the Broadest Waveband Light Harvesting," Adv. Opt. Mater. **1**(1), 43–49 (2013).
26. W. W. Zhang, H. Qi, A. T. Sun, Y. T. Ren, and J. W. Shi, "Periodic trapezoidal VO2-Ge multilayer absorber for dynamic radiative cooling," Opt. Express **28**(14), 20609–20623 (2020).
27. Z. Li, L. Stan, D. A. Czaplewski, X. Yang, and J. Gao, "Wavelength-selective mid-infrared metamaterial absorbers with multiple tungsten cross resonators," Opt. Express **26**(5), 5616–5631 (2018).
28. Y. Zhou, Z. Liang, Z. Qin, X. Shi, D. Meng, L. Zhang, and X. Wang, "Broadband long wavelength infrared metamaterial absorbers," Results Phys. **19**, 103566 (2020).
29. S. Yue, M. Hou, R. Wang, H. Guo, Y. Hou, M. Li, Z. Zhang, Y. Wang, and Z. Zhang, "Ultra-broadband metamaterial absorber from ultraviolet to long-wave infrared based on CMOS-compatible materials," Opt. Express **28**(21), 31844–31861 (2020).

Optics EXPRESS

30. C. Hu, X. Li, Q. Feng, X. N. Chen, and X. Luo, "Investigation on the role of the dielectric loss in metamaterial absorber," Opt. Express **18**(7), 6598–6603 (2010).
31. F. Gervais, "Handbook of Optical Constants of Solids ii," (1985).
32. A. D. Rakić, A. B. Djurišić, J. M. Elazar, and M. L. Majewski, "Optical properties of metallic films for vertical-cavity optoelectronic devices," Appl. Opt. **37**(22), 5271–5283 (1998).
33. J. Li, J. Li, H. Zhou, G. Zhang, H. Liu, S. Wang, and F. Yi, "Plasmonic metamaterial absorbers with strong coupling effects for small pixel infrared detectors," Opt. Express **29**(15), 22907–22921 (2021).
34. F. Ding, J. Dai, Y. Chen, J. Zhu, Y. Jin, and S. I. Bozhevolnyi, "Broadband near-infrared metamaterial absorbers utilizing highly lossy metals," Sci. Rep. **6**(1), 39445 (2016).
35. X. Xu, Y. Li, B. Wang, and Z. Zhou, "Prediction of multiple resonance characteristics by an extended resistor-inductor-capacitor circuit model for plasmonic metamaterials absorbers in infrared," Opt. Lett. **40**(19), 4432–4435 (2015).
36. Y. Q. Ye, Y. Jin, and S. He, "Omnidirectional, polarization-insensitive and broadband thin absorber in the terahertz regime," J. Opt. Soc. Am. B **27**(3), 498–504 (2010).
37. W. L. Barnes, A. Dereux, and T. W. Ebbesen, "Surface plasmon subwavelength optics," Nature **424**(6950), 824–830 (2003).